Real-Time Early Detection of Crack Propagation Precursors in Delayed Fracture of Soft Elastomers

Jianzhu Ju, Gabriel Sanoja, Med Yassine Nagazi, Luca Cipelletti, Zezhou Liu, Chung Yuen Hui, Matteo Ciccotti, Tetsuharu Narita, Costantino Creton

Real time early detection of crack propagation precursors in delayed fracture of soft elastomers

Jianzhu Ju [a], Gabriel E. Sanoja [a,b], Med Yassine Nagazi [c,g], Luca Cipelletti [c,d], Zezhou Liu [e], Chung Yuen Hui [e,f], Matteo Ciccotti [a], Tetsuharu Narita[*,a,f], Costantino Creton[*,a,f]

[a] Sciences et Ingénierie de la Matière Molle, CNRS UMR 7615, ESPCI Paris, PSL Université, 75005, Paris, France

[b] McKetta Department of Chemical Engineering. The University of Texas at Austin. Austin, TX 78723, USA.

[c] Laboratoire Charles Coulomb (L2C), University of Montpellier, CNRS, 34095, Montpellier, France

[d] Institut Universitaire de France, 75231, Paris, France

[e] Sibley School of Mechanical and Aerospace Engineering, Cornell University, Ithaca, NY 14853, USA

[f] Global Station for Soft Matter, Global Institution for Collaborative Research and Education, Hokkaido University, 060-0808, Sapporo, Japan

[g] Present address: Formulaction, 31200 Toulouse, France

Abstract

Fracture of materials can take place below the critical failure condition via the slow accumulation of internal damage followed by fast crack propagation. While failure due to subcritical fracture accounts for most of the structural failures in use, it is theoretically challenging to bridge the gap between molecular damage and fracture mechanics, not to mention predicting the occurrence of sudden fracture, due to the lack of current non-destructive detection methods with suitable resolution. Here, we investigate the fracture of elastomers by using simultaneously space- and time-resolved multispeckle diffusing wave spectroscopy (MSDWS) and molecular damage mapping by mechanophore. We identify a fracture precursor that accelerates the strain rate field over a large area (cm^2 scale), at considerably long times (up to thousands of seconds) before macroscopic fracture occurs. By combining deformation/damage mapping and finite element simulations of the crack-tip strain field, we unambiguously attribute the macroscopic response in elastic deformation to a highly localized molecular damage that occurs over a ~ 0.01 mm^2 sample area. By unveiling this mechanism of interaction between the microscopic molecular damage and the minute but long-ranged elastic deformation field, we are able to develop MSDWS as a flexible, well-controlled tool to characterize and predict microscopic damage well before it becomes critical. Tested using ordinary imaging and simple image processing, MSDWS predictions are proven applicable for unlabeled and even opaque samples under different fracture conditions.

*correspondence authors: tetsuharu.narita@espci.fr
*correspondence authors: costantino.creton@espci.fr

I. Introduction

Resistance to fracture of soft materials is typically characterized with a tensile test carried out until fracture, where parameters such as stretch and stress at break are commonly used. The fracture mechanics community has long used pre-notched samples and defined the fracture energy, Γ in J/m^2, as the critical value of the strain energy release rate G_c, where the crack begins to propagate from the notch [1]. However, careful examination of the experimental data shows that for soft materials, where dissipation takes place over several length and time scales, this critical transition is not very well defined, due to the presence of some slow subcritical crack propagation, and depends strongly on the precision of the measurement. Not only can the strain energy release rate G be time-dependent due to viscoelasticity of the polymer networks [2], the fracture energy Γ can also evolve with the accumulation of localized damage by fatigue [3,4], even though the latter is commonly excluded in models, due to theoretical complexity and the lack of experimental methods to characterize it [5,6]. When $G < G_c$, catastrophic fracture can still take place after a long induction time, a phenomenon known as delayed fracture [2,7,8]. Even in continuous loading conditions, where a notched sample is stretched at a constant rate, it has been commonly observed that there exists a transition from an almost undetectable crack propagation to a fast propagation mode [9-11]. Conventionally, G_c is defined as the critical energy release rate at which this transition occurs. Subcritical damage phenomena occur for $G < G_c$ [2,6] and share the same implicit hypothesis: the almost unpredictable macroscopic failure is due to the progressive accumulation of molecular damage, which may or may not be concomitant with slow subcritical crack propagation [8]. These forms of localized subcritical damage account for most of the catastrophic fracture events in real life, so that the interesting and important question to address is how the transition from slow or no propagation to rapid propagation takes place, and how this transition is related to molecular damage. The goal of the present study is to investigate and understand the precursors of fracture and the early stages of crack propagation by combining the recently developed quantitative characterizations and analysis of molecular damage in elastomers [12] with a method of early detection of nanoscale motion with high temporal and spatial resolution [13].

Light scattering methods such as Dynamic Light Scattering (DLS, for weakly scattering samples [14]) and Diffusing Wave Spectroscopy (DWS, for turbid samples [6,15-18]) can detect motion on the nano-to-micron scale and on sub-millisecond time scales. Conventional DLS and DWS measurements are performed in the far-field geometry, where the detector receives light scattered from the entire illuminated sample. Furthermore, DLS and DWS use a single detector collecting the signal from a few speckles of scattered light at most. Accordingly, they lack spatial resolution and require extensive time average, two features that make them unsuitable for systems where the dynamics are spatially heterogeneous and evolve in time, as in fracture studies. The so-called multispeckle variants of DLS and DWS (MSDLS and MSDWS, respectively) introduced in the last two decades and based on pixelated detectors, relax the time average constraint and allow for time-resolved [19] or even space- and time-resolved measurements [13].

A few studies used MSDLS to detect precursors of failure in soft solids by monitoring the evolution of the microscopic dynamics. The authors of Ref. [20] used time-resolved MSDLS coupled to rheology to investigate the delayed yielding of a colloidal gel under creep. A transient acceleration of the microscopic dynamics was seen and was attributed, quite generically, to a “burst of microscopic plastic rearrangements”. Because that experiment lacked spatial resolution and due to the relatively large length scales probed by single scattering (on the order of one μm), it was not

possible to gain a deeper understanding of the origin of the light scattering signal. Similarly, a MSDLS investigation on a polymer hydrogel [21] revealed what was interpreted as a "wave of plastic activity" preceding failure, but once again the origin of the light scattering signal could not be elucidated.

Several works [6,13-16] used MSDWS to study failure of (partially) amorphous systems, such as elastomers [6], semi-crystalline polymers [17] and granular materials [22], where plastic rearrangements, commonly corresponding to a smooth yielding [23], occur before structural failure. As compared to other methods such as MSDLS or digital image correlation [16,18], MSDWS is particularly appealing thanks to its superior sensitivity to very small motion, down to the nm scale. Quite generally, these works revealed enhanced, spatially heterogeneous microscopic dynamics in materials loaded beyond the mechanical linear regime. In particular, Van der Kooij et al. [6] have applied MSDWS to the investigation of crack growth in an elastomer. By imaging a small portion (a few mm^2) of the sample around a notch and focusing on a time window of a few seconds before rupture, they could detect enhanced dynamics on a single, fast time scale (0.5 ms), just ahead of macroscopic rupture. Unfortunately, that experiment could not address the question of the existence and origin of dynamic precursors, because of the reduced space and time windows that were available and due to blurring effects associated with the transmission geometry that was chosen. More generally, MSDWS experiments are confronted with the challenge of interpreting the physical origin of the measured dynamics. Indeed, a variety of distinct physical mechanisms may lead to similar MSDWS signals, including spontaneous dynamic due to thermal motion, the affine or non-affine deformation of otherwise pristine materials, or irreversible plastic events [18].

These difficulties are particularly challenging in elastomers, where plasticity and yielding are typically not easily observed. In elastomers the absence of a well-defined yield point results in a distinctive type of damage by irreversible bond scission, which has been until recently only characterized macroscopically with cyclic tests showing a softening, the so-called Mullins effect [24,25]. Recently, however, molecular-level insight in failure mechanisms has been gained by inserting mechanophores in the network [12,26-28]. Mechanophores are force-sensitive molecules emitting light or becoming fluorescent upon bond scission. They allow the detection of damaged regions. Mechanophores have revealed that in elastomers bulk molecular damage occurs but only relatively close to the fracture surface [12,26], over distances of the order of tens or hundreds of microns [12,26,29-31].

Crucially, experiments with mechanophores suggest that the bulk of the elastomer remains elastic and intact. This naturally raises the question of the nature of the enhanced dynamics measured by MSDWS in previous experiments [6] over distances seemingly larger than those concerned by bond breaking. More generally, mechanophores provide the unique opportunity to clarify the relationship between the accumulation of localized molecular damage, the enhanced dynamics reported in previous light scattering experiments, and the (delayed) macroscopic failure.

Here, we investigate failure in a mechanically loaded elastomer of polydimethylsiloxane (PDMS), using a unique combination of the detection of localized molecular damage, simultaneous space-resolved measurements of the microscopic dynamics over the whole sample, and finite element simulations [32,33]. We show that while bond breakage is confined to a region up to about 100 μm from the crack tip, it induces a long-ranged strain field ruled by linear elasticity that is detectable by MSDWS up to more than one cm from the crack tip, up to thousands of seconds before macroscopic failure. Finite element simulations support the proposed scenario, ruling out ultraslow crack propagation as an alternative source of the

MSDWS signal.

Collectively, our experiments and modelling provide unique insights on the long-range effects of molecular damage, clarifying the microscopic origin of the enhanced dynamics measured by MSDWS. Together with tests on a variety of materials under different loading conditions, they allow establishing on firm bases MSDWS as an effective, versatile method for detecting and anticipating catastrophic crack growth and material failure.

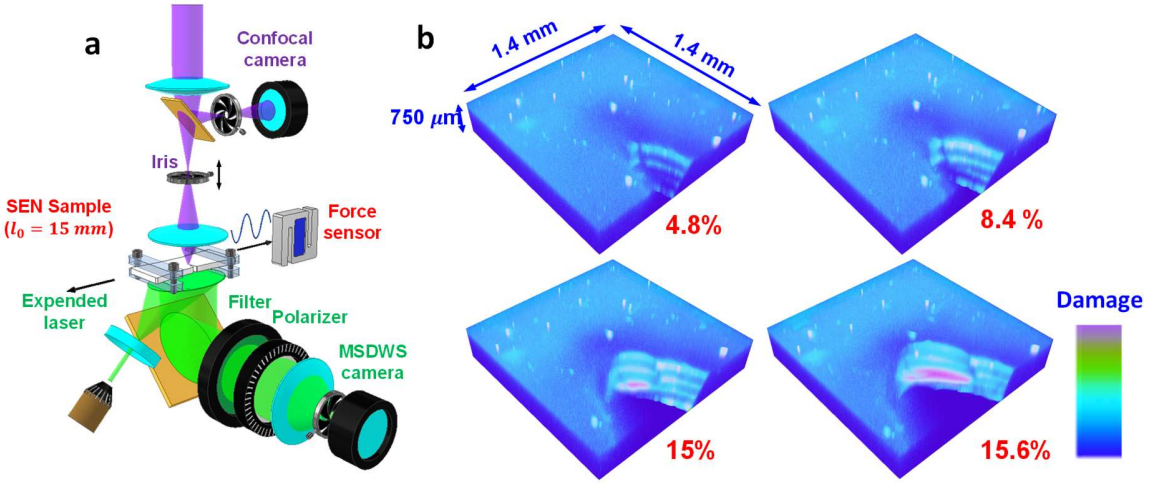

FIG. 1 (a) Set-up for simultaneous MSDWS and confocal microscopy. A single edge notched sample (width 9 mm, length 15 mm, thickness 2 mm and notch length 1 mm, cut with a fresh razor blade) is tested under uniaxial tension simultaneously mechanically, by MSDWS, and by confocal microscopy. (b) 3D image of bonds breaking around the crack tip during tensile testing of a notched PDMS sample. 4 image slices (1.4 mm × 1.4 mm in plane with detection thickness 150 μm) scanning a depth of 750 μm around the midplane of the sample are collected for one single 3D image. Images are labelled by the imposed strain.

II. Simultaneous mapping of strain rate and damage

Sylgard 184 polydimethylsiloxane (PDMS) is used as a model soft material, with a pi-extended anthracene Diels-Alder adduct diacrylate [34] (0.1 wt%) used as a mechanophore cross-linker and TiO_2 nanoparticles (diameter 250 nm, 0.25 wt%) dispersed before curing (**APPENDIX A**). Single edge notched (SEN) samples were tested in uniaxial tension until failure with a nominal stretch rate $\dot{\varepsilon}_N = 5\times10^{-5}\ s^{-1}$, in a custom-designed tensile rig, with both clamps moving symmetrically in opposite directions, and fitted with the experimental set-up shown in FIG. 1(a). A spatially resolved characterization of the dynamics over the whole sample surface was carried out by MSDWS in a backscattering geometry, by illuminating the sample from the bottom with a expanded laser beam. The technique detects motion in a sample slab of thickness several l^* ($l^* = 430\ \mu$m) the photon transport mean free path. In the present case, this corresponds to about 20% of the sample thickness. Simultaneously, fluorescence from the broken mechanophores crosslinkers was detected by confocal imaging from the top, around the crack tip. Under continuous stretching, PDMS has a Young's modulus around 1.2 MPa (FIG. S1, **supplemental material**) and macroscopic fracture is detected in SEN samples at a nominal strain $\varepsilon_f = 15 \sim 16\%$, as detectable from bright field imaging.

FIG. 1(b) shows the 3D mapping by confocal microscopy of the fluorescence

intensity due to the mechanophore activation around the original open notch, for different levels of crack opening related to applied strains. Briefly, as the sample is stretched, some of the crosslinker molecules break near the crack tip. When the mechanophore cross-linker is irreversibly broken, it becomes fluorescent under laser illumination, so that the accumulated bond scission can be measured by confocal microscopy [12,35]. Previous work on poly ethyl acrylate networks [12] has shown that within this concentration range, and provided that the mechanophore is used as a crosslinker and is well soluble in the elastomer (which is the case here), the fluorescence intensity is proportional to the number of crosslinkers undergoing scission. The high quantum yield of the pi-extended anthracene gives a detection limit of the order of 1 ppm relative to monomer unit. However, the random incorporation and activation of the mechanophore should be tested when incorporated into a completely new material.

To build each 3D image, 4 image slices are collected (**APPENDIX A**) and the dark strip patterns in the 3D images correspond to the gaps between slices, not to structure. In the shown experiment, fracture is observed at ε_f = 15.6 %. While initial activation is due to the artificial cut of the notch, images show that the activation intensity due to bond breaking increases already at strains much lower than ε_f (from 4.8% to 15%). At small $\varepsilon_N < 13\%$, the majority of the activation that is observed is mainly due to the cutting of the notch with a sharp razor blade and does not extend beyond 50 μm away from the tip of the notch. From the onset of propagation (ε_N =15 % in FIG. 1(b)), massive damage is detected around the crack in the 3rd slice, with length over 500 μm along the crack profile.

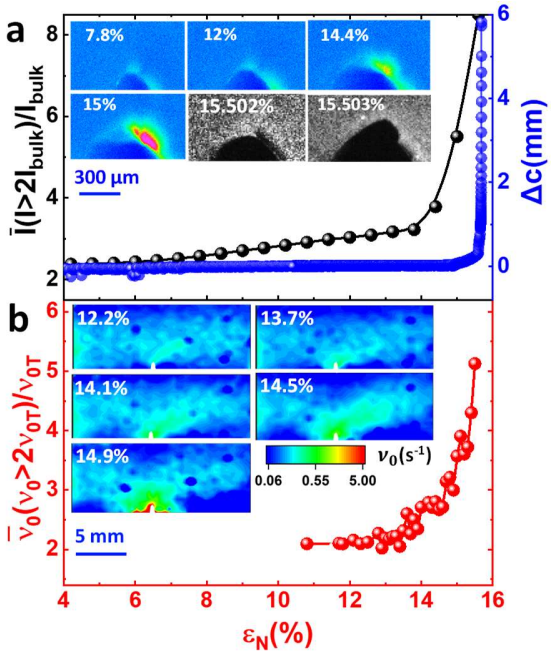

FIG. 2(a) Main plot: Black, Averaged intensity $\bar{I}$ of mechanophore activation, in the region with $I > 2I_{bul}$ (defining activated fluorescence after deformation), renormalized by the bulk intensity I_{bulk}; Blue: crack propagation length Δc. Insets: 2D mechanophore maps at 400 µ m deep from the sample surface. For images at the onset of macroscopic propagation (15.502 % and 15.503 %), confocal microscope cannot capture the images due to its low time resolution, so that raw images from the MSDWS camera are shown instead. (b) Main plot: Averaged value of the normalized relaxation rate $\bar{\nu}_0/\nu_{0T}$ (red) measured by MSDWS in the region $\nu_0 > 2\nu_{0T}$. Inset: ν_0 maps at different ε_N. Note that the field of view in MSDWS is about 20 times wider than in confocal microscopy.

Area-averaged fluorescence intensities $\bar{I}$ were calculated in the 3rd slice, within the region where $I > 2I_{\text{bulk}}$, where I_{bulk} is the average fluorescence intensity in a region far away from the crack tip (see **supplemental material** for detail). $\bar{I}$ is then renormalized by I_{bulk} to remove the influence of absorption and laser bleaching, as shown in FIG. 2(a). From the beginning of stretching, $\bar{I}/I_{bulk}$ increases slowly at an almost constant rate for $\varepsilon_N <$

14 %. At ε_N = 14.4 % ($\Delta t = 240$ s before fracture), a larger increase in intensity occurs on the right side of the crack in the 2D image (inset of FIG. 2(a)), after which $\bar{I}/I_{bulk}$ increases faster. For 13.8 % < ε_N < 15.1 %, there is a rapid increase in fluorescence intensity, but no crack propagation is detectable by bright field microscopy imaging with sub-micron resolution. As seen in FIG. 2(a), a slight change in crack length Δc is detectable only starting at $\varepsilon_N = 15.1$ % ($\Delta t = 100$ s before fracture), when the crack starts growing at an ultraslow rate ~ 1.5 μm/s. A sharper crack is then nucleated 19 s before macroscopic fracture (~ε_N =15.5%), at a location which matches well the region where molecular-level damage was already visualized by mechanophore mapping at smaller strains. Note that 90 % of the crack propagation occurs in the last 5 s, making it extremely difficult to anticipate macroscopic fracture by conventional imaging alone.

MSDWS was used simultaneously to map spatially the microscopic dynamics, by imaging the bottom face of the sample. Briefly, a characteristic relaxation rate ν_0 of the microscopic dynamics was obtained by fitting the temporally and spatially resolved intensity autocorrelation function, where larger ν_0 values correspond to faster dynamics (see **APPENDIX A** and **supplemental material**). Maps of ν_0 were built for different values of ε_N during the continuous stretching experiment and are shown in FIG. 2(b). For ε_N < 13.7 %, the ν_0 maps remain almost identical, with slightly higher values of ν_0 around the crack tip, where the faster dynamics region progressively develop to the right, consistent with the molecularly damaged region detected by fluorescence confocal microscopy in FIG. 2(a). For ε_N > 13.7 % ($\Delta t = 380$ s before fracture), a significant acceleration of the dynamics occurs in front of the crack and grows rapidly.

Crucially, by coupling the MSDWS measurements to the mechanophore signal, we can interpret quantitatively the light scattering data. The confocal images show that crosslinker scission is localized within ~200 μm from the crack tip. The enhanced dynamics detected by MSDWS occurs over a much larger region (~1 cm from the tip), where the network is intact. Thus, the MSDWS signal must correspond to the elastic response of the pristine elastomer network to localized breakage, rather than to structural changes directly resulting from widespread bond scission. With this in mind, we can now relate the MSDWS measurements to the long-range strain rate field induced by the bond breaking events localized near the crack tip. It can be shown (see **supplemental material**) that measured dynamics under these conditions can be well described by $\nu_0 = \sqrt{3} k l^* \sqrt{\mathrm{Tr}(\boldsymbol{D}^2)}$, where k is the laser light wave vector and $\boldsymbol{D}$ is the symmetric part of the velocity gradient tensor in the deformed state (namely, the rate of deformation tensor [18,36-38]). The absolute strain rate value corresponding to the measured ν_0 can be calibrated by determining the setup and sample-dependent constant kl^* in uniformly deformed, un-notched samples [18], where ν_0 is proportional to the true strain rate along the stretch direction, $\dot{\varepsilon}_T$ (see **supplemental material**). An applied $\dot{\varepsilon}_N$ = 5×10^{-5} s^{-1} corresponds to ν_{0N} = 0.23 s^{-1} and $\dot{\varepsilon}_T$ corresponds to $\nu_{0T} = \nu_{0N}/(1 + \varepsilon_N)$. Since ν_0 is proportional to the (local) train rate, here and in the following we shall use it as a proxy for the deformation rate. The averaged value $\bar{\nu}_0$ in the region with $\nu_0 > 2\nu_{0T}$ (roughly, the green region in the

maps in the inset of FIG. 2 (b)) is calculated and shown in FIG. 2(b), after normalization by ν_{0T} . $\bar{\nu}_0/\nu_{0T}$ start increasing at ε_N = 13.5 % ($\Delta t = 420$ s before fracture) and reaches a large value of 4 at ε_N=15 %, where the area with $\nu_0 > 2\nu_{0T}$ extends over 10 mm^2.

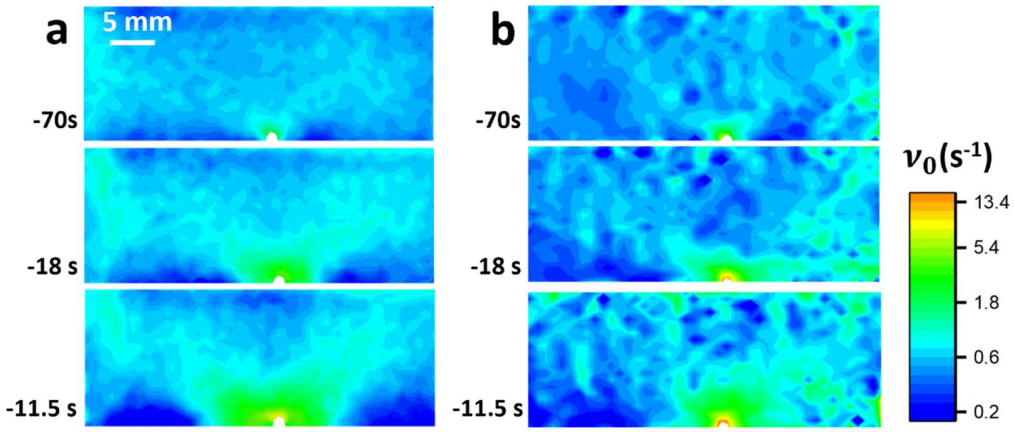

FIG. 3 Maps of the relaxation rate ν_0 calculated from MSDWS (a) and DIC (b) at different times before fracture for two distinct samples stretched at $\dot{\varepsilon}_N = 1.25\times10^{-4}$ s^{-1}.

As a further demonstration that in our experiments the MSDWS dynamics is modified by the long-range strain rate field set by localized damage, we compare the MSDWS results to a more conventional quantification of the strain field obtained, on a separate sample, by a classical digital imaging correlation method (DIC). The MSDWS and DIC tests followed the same protocol: different samples with identical geometries (size 2 cm × 4 cm × 4 mm, crack length c = 2 mm) were subjected to uniaxial extension at $\dot{\varepsilon}_N = 1.25\times10^{-4}$ s^{-1} until failure. DIC measures spatially resolved deformation fields by comparing images of the sample surface during the elongation test. In order to resolve all components of the 2D strain rate tensor $\boldsymbol{D}$, the sample is sprayed with black ink, which forms a speckled pattern, whose displacement is then tracked. $\boldsymbol{D}$ is calculated with images collected from time t to $t+T$ (by program customized from open source project pydic [39], see **supplemental material** for details), where T is the time interval for correlation and averaging.

Due to the lower detection sensitivity of strain heterogeneity of DIC, the minimum required time T_{min} between images to obtain a reliable signal is much longer compared to the $\tau_0 = 1/\nu_0$ (~0.2 s) around the crack tip, the characteristic decorrelation time of the autocorrelation function. In FIG. 3(b), we applied $T = T_{min}$, which are 20 s, 10 s and 4 s, respectively.

For the sake of comparison with MSDWS, the strain rate tensor obtained by DIC is used to calculate the relaxation rate $\nu_0(\boldsymbol{D})$, i.e., the same quantity that is directly measured by MSDWS. The ν_0 maps obtained by MSDWS and DIC are shown in FIGs. 3(a) and 3(b), respectively, for the same times before full fracture (the sample tested with MSDWS failed at ε_f =15.9 % while the sample tested by DIC failed at ε_f =15.7 %). The quantitative similarity between both maps is evident, thus confirming that the dynamics measured by

MDWS are due to modifications of the long-range strain field induced by localized bond breaking and validating the use of MSDWS to quantitatively map strain rate, including in a complex 2D geometry with a notch.

To summarize, both mechanophore mapping of molecular damage and MSDWS dynamics mapping show that during a long induction period, from around $\varepsilon_N \sim 13.5$ % to just before the rapid crack propagation, there are detectable microscopic precursor events, whose characteristic size progressively grows, while no macroscopic failure occurs. Remarkably, while bond breaking occurs only very close to the crack tip, over a ~ 0.01 mm^2 sample area, the resulting strain field can be simultaneously detected by MSDWS and DIC over a much larger area, of the order of the sample size ~ 20 mm^2. At the stretch rate applied here, the precursors highlighted by both methods are observable about 7 min before macroscopic fracture, clearly demonstrating their predictive power.

III. Finite element modelling rules out any contribution of slow crack propagation to the strain field

Naturally, localized damage plays an important role in crack propagation, but in existing continuum models it is theoretically challenging to couple damage and deformation [40]. An important question raised by our experiments is whether the increase in strain rate measured by MSDWS far from the crack tip is i) due to the combined effect of sample loading and of a slow crack growth that may go undetected because of image resolution limitations; or ii) is the result of the localized molecular damage detectable by fluorescence. To address this question, we carried out for the same model PDMS a full-field finite element method (FEM) simulation. It must be noted that the FEM simulation considers only the contribution of deformation and crack propagation and does not account for changes in local material properties due to molecular-level damage. We used a neo-Hookean solid material model [41] with parameters fitted to the uniaxial tension data to calculate the full-field strain rate. To examine whether the measured increase in strain rate is due to undetectable slow crack growth, we performed an FEM simulation with a stationary crack and with a slowly growing crack at different speeds, respectively. Propagation is simulated by introducing an increasing crack length from the stationary crack position, otherwise leaving all material properties unchanged. The FEM results are compared to the DIC measurements described in the previous section, by plotting the strain rate along the stretching direction, $D_{\mathrm{xx,FEM}}$ and $D_{\mathrm{xx,DIC}}$ for FEM and DIC respectively, as a function of y, for fixed $x = 0$ (see inset in FIG. 4(a)).

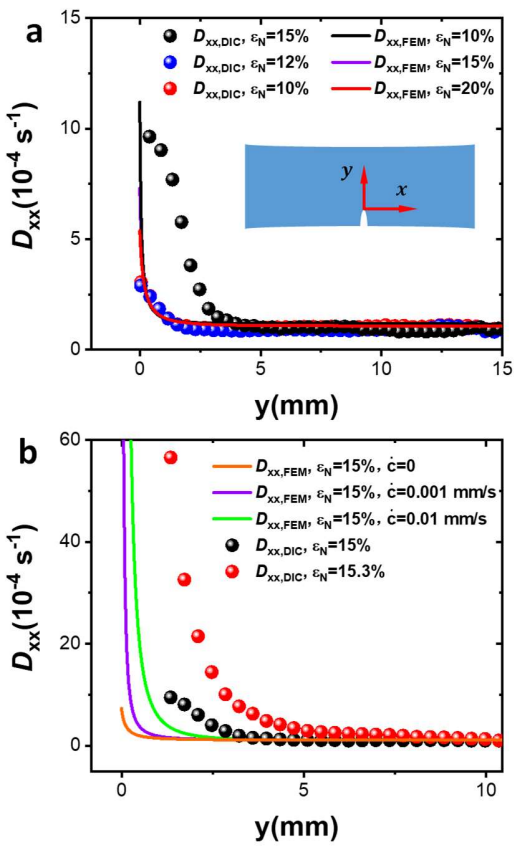

FIG. 4 (a): $\boldsymbol{D}_{xx}$ component of the rate of deformation tensor as a function of distance y from the crack tip, for x = 0 (see scheme in (a)), as obtained by DIC (symbols, experiments) and FEM (lines, simulations). In (a), FEM data were obtained assuming that the crack tip does not move. (b): Same as in (a), but focusing on the late stages of the tests and implementing crack tip propagation in FEM, at various propagation speeds ċ, as indicated by the labels.

Results without and with crack propagation are shown in FIGs. 4(a) and 4(b), respectively: in both cases, $\dot{\varepsilon}_N$ = 1.25 × 10^{-4} s^{-1}. In the absence of propagation, $D_{\mathrm{xx,FEM}}$ far from the tip ($y >$ 0.1 mm) remains almost the same up to ε_N ~20 % (the sample does not break in simulations). However, while at low strain the experimental $D_{\mathrm{xx,DIC}}$ and numerical $D_{xx,FEM}$ match well, starting from ε_N = 15 %, $D_{xx,DIC}$ is significantly larger than $D_{xx,FEM}$, even millimeters ahead of the tip, without any experimentally detectable propagation of the crack, indicating the existence of a fracture precursor, as discussed in relation to FIG. 2. In FIG. 4(b), we use our FEM result to test whether the strain rate field measured in experiments could be due to crack propagation alone. Even if one assumes a crack speed $\dot{c}$ = 0.01 mm/s in the simulation (one order of magnitude above the optically detectable crack speed $\dot{c} \sim$ 0.001 mm/s) $D_{\mathrm{xx,DIC}}$ is still well above $D_{xx,FEM}$ at ε_N = 15 % (FIG. 4(b)). Furthermore, at a slightly larger strain of ε_N = 15.3 % (24 s later), still without any experimentally detectable crack propagation, a dramatic increase of $D_{\mathrm{xx,DIC}}$ is observed, once again not captured by FEM.

In summary, at small values of applied ε_N, the comparison between simulation (FEM) and experiments (MSDWS/DIC) shows excellent consistency. However, for higher values of ε_N approaching macroscopic fracture, the experimental values deviate largely from FEM simulations. These results, combined with the MSDWS and mechanophore mapping, demonstrate that the acceleration of the local strain rate over a large sample volume corresponds to the elastic response of the material to chemical bond scission localized very close to the crack tip. While ε_N itself influences significantly D_{xx} only in a region very close to the crack tip (FIG. 11, **APPENDIX B**), the rapid growth in strain rate before fracture shows a strong instability in response of dynamic damage accumulation. Note that the damage accumulation can be observed at lower ε_{N} (FIG. 2(a)), but only leads to an acceleration of the strain rate and fracture after ε_{N} >13.5 %, suggesting a threshold level of damage above which propagation can be initiated. This threshold of damage level appears distinct from that predicted

by the *Lake–Thomas* model [42], which considers bond scission only over one network mesh size (10 nm) ahead of the crack as the threshold [43]: in our experiments, by contrast, the damage zone size extends over a distance of about 200 μm (FIG. 2(a)) from the fracture surface. This may be due to the well-known presence of silica nanoparticles in the Sylgard 184 that delocalize the damage [44]. More generally, our findings highlight the crucial need to include the effect of bond scission, which is absent from most FEM models, and typically not considered in similar theoretical [2,5] and experimental works [6,7] addressing subcritical fracture.

IV. Damage prediction with MSDWS dynamic activity maps

1. Damage prediction in continuous condition

The observation of the large-scale strain rate acceleration in response to a damage close to the crack tip suggests that damage may be predicted, and thus prevented, by inspecting only the elastic response by MSDWS at a very early stage and far from the crack tip, before the appearance of any macroscopic structural failure. Note that in principle full-field DIC can provide similar information in terms of strain (rate) distribution, but the raw output of DIC is the displacement field of the grid elements into which the sample image is divided. The resolution depends on the spray-painted speckle quality, resulting in a strain precision around 10^{-3} [45-48]. By contrast, MSDWS detects directly the intensity time decorrelation due to the change in strain tensor in the deformed configuration [17], providing a strain precision up to 10^{-6} [18]. Also, compared to painted speckles, laser speckles are independent of the deformation scale, so that even the large strain regime can be well captured [17]. For hydrogels or emulsion systems with a high volume fraction of liquid, MSDWS provides an alternative method to measure the magnitude of the displacement without the need for spray painting [49]. Finally, MSDWS typically requires a shorter time than DIC to obtain a signal. We introduce therefore an alternative to strain rate mapping, by calculating only the correlation values calculated at one single time lag, τ_{MSDWS}, to build dynamic activity maps (DAMs) [13,18]. The time needed to build a DAM in our experiments (typically $\tau_{MSDWS} \sim 0.05/\nu_0$ is required), is ~ 100 times faster than what is required to obtain the same information by DIC, since only a simple calculation between two images is required to visualize the transient strain rate distribution.

We realized a prototype test on a mechanophore-labelled PDMS sample with five nominally identical notches, as shown in FIGs 5(b,c,d), stretched at $\dot{\varepsilon}_N = 5 \times 10^{-5}$ s^{-1} according to the protocol illustrated in FIG. 5(a). Each notch is cut with a fresh blade (scalpel blades #11) to exclude as much as possible the additional influence from variation in crack geometry. We processed the speckle images in real time, obtaining DAMs simultaneously to the mechanical test, using $\tau_{MSDWS} = 0.75$ s. Including the time for DAM computing and image saving (for later reference), an optimized time resolution of 1 s is achieved. The DAMs are visually inspected on the fly to monitor local damage and stretching is stopped when a precursor is identified.

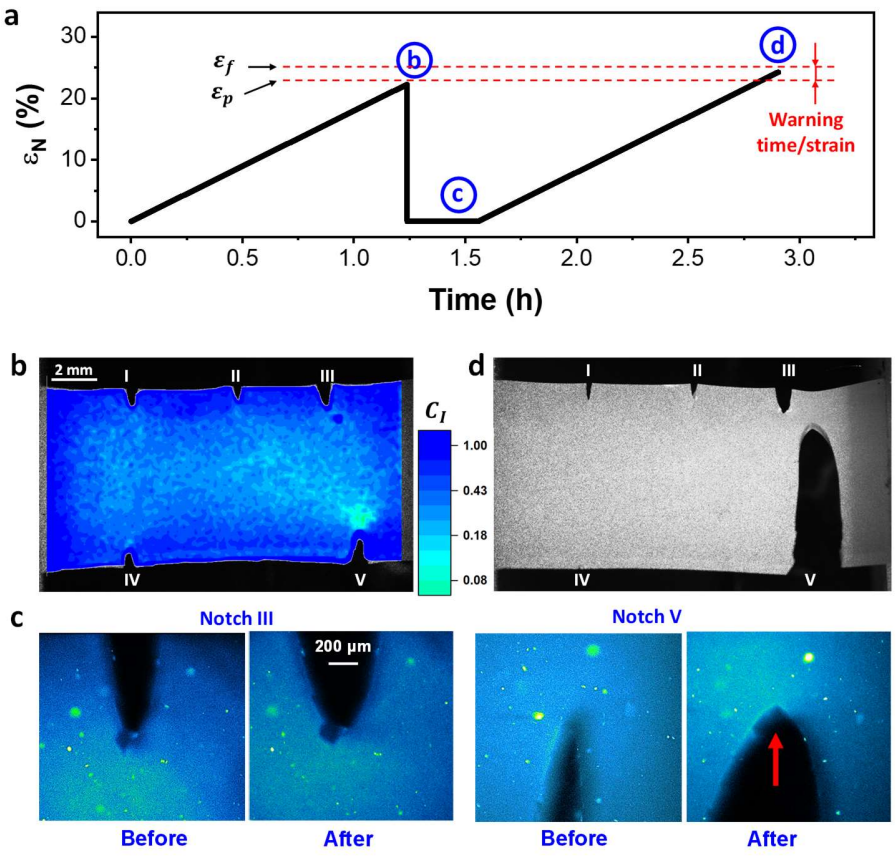

FIG. 5(a) Prototype test of the predictive capability of MSDWS. Letters corresponding to maps taken at different stages of the experiment are indicated in the strain-time curve. For both stretching ramps, the strain rate is $\dot{\varepsilon}_N = 5\times10^{-5}\ s^{-1}$. (b) Real-time DAM obtained at $\varepsilon_N = 22.3\% = \varepsilon_p$, using $\tau_{MSDWS} = 0.75\ s$. The DAM reveals the formation of a dynamic precursor localized ahead of notch V. (c) Mechanophore mapping after unloading: notch III (for which the DAMs showed no enhanced dynamics) and V (for which the DAMs did show enhanced dynamics) after the first stretching ramp ($\varepsilon_N = \varepsilon_p$), compared to the pristine sample ($\varepsilon_N = 0$) as a reference. The sample was slightly opened (much less than ε_p) for a better visualization of activation. (d) Final fracture during the second loading ramp, at a strain $\varepsilon_f \sim \varepsilon_p + 2\%$. (see horizontal dashed lines in a))

Like the results in FIG. 2(b), a dynamic precursor is seen during the first loading ramp, here at a strain ε_p = 22.3 % (for multiply notched samples, the strain at failure ε_f is found to be larger than that for samples with one single notch). Remarkably, significant differences between the five notches can be detected: at ε_p = 22.3 %, only notch V is accompanied by a fast dynamic region, reaching a size ~ 2 mm^2 (FIG. 5(b)). As soon as the DAMs reveal a dynamic precursor, the stretching ramp is stopped and the sample is unloaded and removed from the tensile stage for inspection of the five notches under confocal microscopy. The results for notch III and V are shown in FIG. 5(c), which compares the mechanophore signal for the pristine sample, before any loading, to that after the first stretching ramp. Obvious activation can only be detected in front of notch V, the same that displayed a fast dynamics region in the DAM. Upon

reloading (second strain ramp in FIG. 5(a)), the final fracture occurs at notch V (FIG. 5(d)), as suggested by the localization of the fast dynamics previously measured with real-time DAMs.

When repeating the similar experiment, but stopping the second stretching ramp at the precursor strain ε_p and then holding the sample at fixed strain, the crack never propagated within an observation time of one hour. By contrast, when applying the same protocol of FIG. 5(a) (*i.e.,* loading the sample until fracture during the second stretching ramp), we found a strain at fracture ε_f around 2% larger than the precursor strain ε_p. We conclude that the occurrence and location of macroscopic failure is successfully predicted, with a warning in macroscopic strain of 2 % (400 s in time with our strain rate), at the stage where only a very small amount of molecular damage can be observed by confocal microscopy (FIG. 5(c)). Several repetitions of the experiments are shown in FIG. S12 and S13 in **Supplemental material**.

2. Damage prediction in static condition

Note that we reported here the predictive capacity of MSDWS for notched samples under continuous loading: a test protocol designed to predetermine, to some extent, both the location and time (or strain) of macroscopic failure. In real-life applications, one is more interested in: i) Long time delayed (hours or even days) fracture under low external loading; ii) The detection of an internal flaw at an *a priori* unknown location, rather than at an artificial notch.

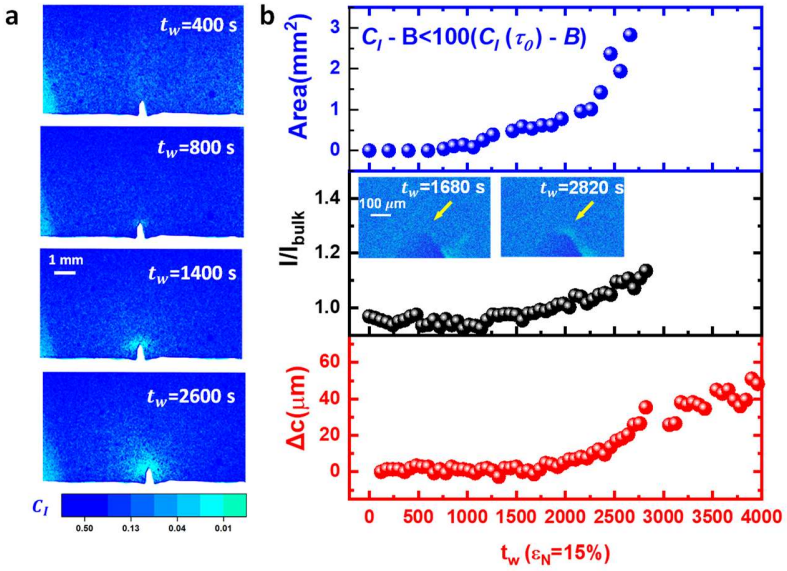

FIG. 6 (a) Dynamic activity maps (DAMs) obtained by plotting C_I values from MSDWS at different waiting times t_w, with a fixed τ_{MSDWS} = 40 s. (b) Time evolution of precursors of failure inferred from MSDWS (top), mechanophore signal (middle), and crack imaging (bottom), respectively. Top: Area in the DAM where the dynamics are much faster than in the bulk, see text for definition; middle: renormalized fluorescence intensity due to mechanophore activation I/I_{bulk}; bottom: propagation length of the crack as a function of t_w. Inset of the middle panel: 2D confocal images showing the mechanophore signal at 1680 s and 2820 s, respectively.

To test the predictive power of MSDWS under those conditions, the evolution of

the molecular damage and of dynamics localization are simultaneously observed in a situation where SEN and un-notched samples are stretched to different strains in a step-by-step fashion and held there for measurement, with a long waiting period at in-between steps.

In the notched sample, the macroscopic strain is carefully increased by steps of $\Delta\varepsilon_N$=2.5 % maintained for 1h, and above ε_N = 12.5 %, smaller steps ($\Delta\varepsilon_N$ = 0.625 %) still maintained by 1h, are chosen to ensure delayed fracture at a fixed displacement [6,7] instead of fracture during the loading step in uniaxial tension.

At ε_N = 15 % (FIG. 6), a slight propagation is initially detected around t_w = 1800 s (the waiting time t_w is defined as the time elapsed since the end of each displacement step), with ultraslow propagation without fracture after 5 h. The initial growth of the crack is only detectable by mechanophore imaging with sub-micron resolution. On the other hand, DAMs show a fast dynamics region revealing the acceleration of the strain rate around the crack tip, which starts to develop at t_w = 800 s, see FIG. 6(a). Note that for delayed fracture at fixed strain, an experiment where bulk dynamics is dominated by relaxation rather than by strain rate would require a method employing a renormalized τ_{MSDWS} to better visualize crack localization, as discussed in APPENDIX C. At really long t_w as in FIG. 6, bulk dynamics is much slower than crack dynamics, so that a constant τ_{MSDWS} = 40 s can be applied here for simplicity. The area with dynamics much faster than the bulk region (defined as $C_I - \mathrm{B} < 100(C_I(\tau_0) - B)$) is calculated and shown in FIG. 6(b), together with the renormalized damage I/I_{bulk} (of the 50 μ m × 50 μ m area in the eventually damaged region) by mechanophore imaging and the crack length increase Δc. The onset of ultraslow crack propagation ($dc/dt \sim 20$ nm/s) starts at t_w = 1700 s, accompanied by a small increase of I/I_{bulk} revealing a slight increase of fluorescence intensity due to mechanophore activation. The extent and magnitude of the faster dynamic activity in DAMs further develops with t_w, reaching 3 mm² at 3000 s, while the steady propagation stays slow and only reaches 100 μm after 5 hours (FIG. 16). Remarkably, well before the slight crack propagation (Δc < 10 μm) and damage accumulation (~20 μm), the localization signal in DAM is already macroscopically visible, starting from t_w = 800 s.

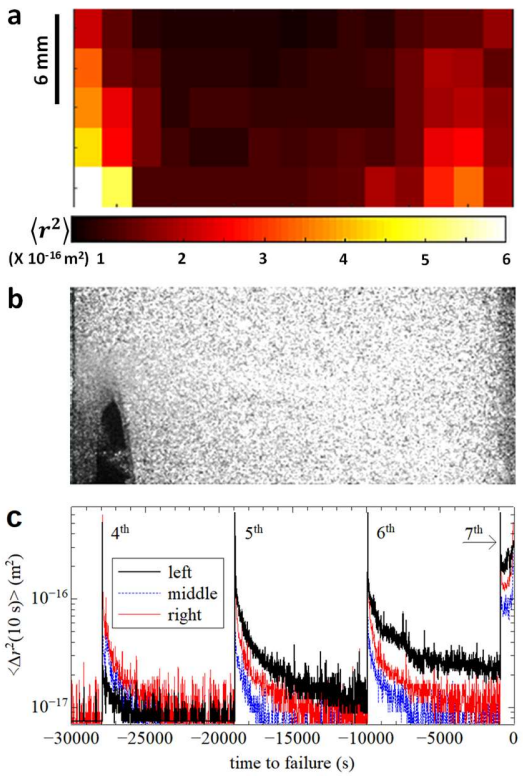

FIG. 7(a) DAM obtained for an un-notched PDMS sample submitted to a series of strain steps, 20 s after imposing the seventh step (ε_N = 23.1%). The DAM is obtained using $\tau_{MSDWS} = 10\,s$. (b): speckle image taken during fast crack propagation, which occurred 910 s after the DAM shown in (a). Note that the crack starts from the bottom left corner of the sample, where the DAM revealed faster dynamics almost 1000 s before. (c) Mean squared displacement $\langle \Delta r^2 \rangle$

over a time delay τ_{MSDWS}= 10 s, averaged over the left-most, the central, and the right most column of the DAM shown in (a), as a function of time before failure. For the sake of clarity, only relaxation phases 4 to 7 are shown. Failure occurs at t = 0 in the figure, about 900 s after the seventh relaxation phase.

A similar behavior is observed in an additional test on an un-notched PDMS sample with a rectangular shape, to avoid *a priori* strain localization. We used here a distinct MSDWS setup (FIG. S14 in **supplemental material**), based on a design similar to that of FIG. 1(a). We impose seven strain steps of nominal strain amplitude 3.3% each, at a strain rate of 3.3×10^{-2} s^{-1}. After each step, the sample is held at a fixed strain for 9000 s and the microscopic dynamics are quantified by DAMs of the microscopic mean squared displacement $\langle \Delta r^2 \rangle$ [15] obtained from the C_I signal, using $\tau_{MSDWS} = 10$ s (see more details in **supplemental material**).

The DAM taken 20s after the beginning of the seventh rest phase (nominal strain $\varepsilon_N = 23.1\%$), shown in FIG. 7(a), reveals enhanced dynamics (larger $\langle \Delta r^2 \rangle$) as compared to those in the initial phases of the experiment, as well as strong spatial heterogeneity. The dynamics are significantly faster close to the grips, suggesting that the sample has been weakened in these regions when it was mounted in the setup, although no signature of potential weakening could be detected macroscopically. Indeed, the act of clamping the sample during tensile tests does induce a stress concentration and this is a long-standing question in experimental mechanics [50,51]. However, while one may expect damage and stress concentration to occur in all four corners of the stretched sample, we find that the dynamics are faster in the bottom part of the left grip ($\langle \Delta r^2 \rangle \sim 6\times10^{-16}$ m^2), precisely where macroscopic failure will eventually occur, almost 1000 s later (FIG. 7(b)).

In order to further demonstrate the predictive power of MSDWS applied to fracture problems, we plot in FIG. 7(c) the time dependence of $\langle \Delta r^2(10\text{ s}) \rangle$ averaged over three sample stripes, near the two clamps and in the middle. Data for the 4th relaxation phase are representative for the behavior at small strains: after each pulling step (identified by the large overshoot of the mean squared displacement), $\langle \Delta r^2 \rangle$ decays over a few thousands of seconds, with no notable differences according to sample area. By contrast, starting from the 5th relaxation phase, the decay of $\langle \Delta r^2 \rangle$ slows down, while dynamic activity is enhanced close to the grips. The 6th relaxation phase confirms this trend, until during the 7th relaxation phase the dynamics near the grips are sped up by almost a factor of ten, and accelerate until sample failure, rather than slowing down as during the previous phases. Starting from the 6th relaxation phase, the dynamics close to the left grip are consistently faster than close to the right grip, providing a warning on where the sample will eventually fail with several thousands of seconds of advance.

Note that in this test the sample is at rest during the relaxation phases, which would make it difficult to obtain a measurable DIC signal, since T_{min}, the required time interval for correlation, would likely become longer than the duration of each step.

Thus, these tests in static condition demonstrate the great sensitivity of MSDWS as a tool to anticipate macroscopic fracture in static subcritical loading. Finally, we note that for these studies, since the bulk dynamics of the material is dominated by relaxation, the correspondence between DAMs and

mechanical parameters is rather complex. In these cases, DAM is only employed as a qualitative visualization to characterize the level of localization.

3. Extension of the method to different materials

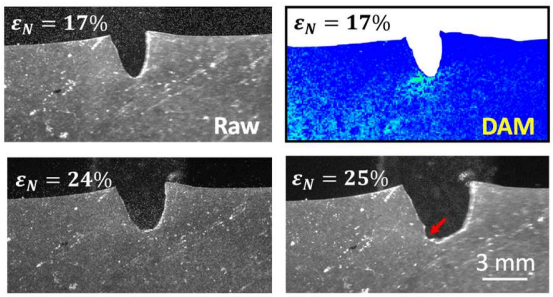

FIG. 8 The prediction of "sideway" propagation in natural rubber.

The detection of a large-scale dynamic precursor was illustrated in the previous sections for a PDMS elastomer, but similar precursors exist in different materials. To demonstrate the generality of the results reported for PDMS, we show in APPENDIX C.1 data for a poly (ethyl acrylate) network, an elastomer with a very standard network structure, but an entirely different chemistry as compared to PDMS. As for PDMS, we find that MSDWS allows for detecting the large-scale elastic response to localized microscopic molecular damage.

MSDWS can detect microscopic damage with excellent temporal resolution, with the only requirement of having a highly scattering material with no strong absorption of light. This is a common feature of many soft materials due e.g. to the presence of fillers or structural features of a length scale of the order of the wavelength of visible light. The method can be used for semi-crystalline polymers [17], filled soft materials [52] or any transparent material to which a small amount of high refractive index probe particles can be added before shaping. We show here two examples of testing the onset of fracture in raw materials, where no added probe particles were necessary. The first example concerns a SEN sample of natural rubber, where impurities provide multiple scattering, which was submitted to uniaxial extension at a rate $\dot{\varepsilon}_N = 2 \times 10^{-4}$ s^{-1} (FIG. 8). A sideway propagation [53] of the crack, classically observed in natural rubber due to strain-induced crystallization [54], is observed at ε_N = 25 %, where the crack starts propagating to the left of the notch (red arrow). Remarkably, a fast dynamics region with a length ~ 2 mm can be already detected precisely in that region by inspecting a DAM measured at ε_N = 17 %, 400 s before any propagation can be detected by direct imaging.

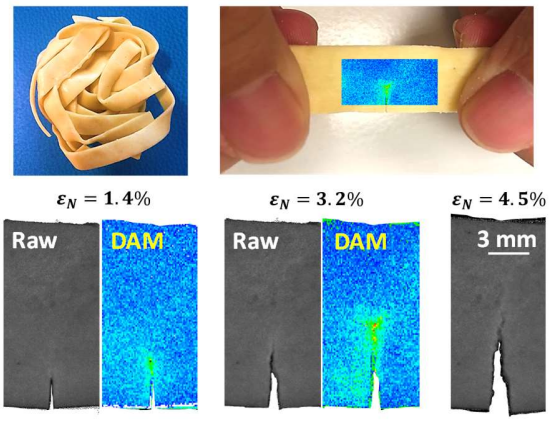

Fig. 9 Raw images and DAMs during the propagation of a piece of notched tagliatelle pasta (with egg).

The second example concerns crack propagation in a piece of notched dry tagliatelle pasta, stretched at $\dot{\varepsilon}_N = 10^{-4}$ s^{-1}, where ductile fracture starts from a very small strain, as shown in FIG. 9. Interestingly, the somehow tortuous propagation path can be well predicted from DAMs collected at lower applied

strain.

Note that in these materials, localized dynamics are not necessarily due to changes in strain rate only, since MSDWS detects multiple contributions to the dynamics [17]. Details of the experiments of FIGs. 8 and 9 are provided in the **supplemental material**.

V. Conclusions

During the fracture of PDMS elastomers, MSDWS reveals an acceleration in local dynamics up to thousands of seconds before macroscopic fracture. Unlike in previous MSDWS works were early detection of failure was not possible [6,17,20], or MSDLS measurements where the microscopic origin of the enhanced dynamics remained unclear [6,17,20,21], here we unambiguously show that the MSDWS signal stems from the global elastic response of the material to local damage. FEM simulations and mechanophore mapping confirm this scenario: the elastic response over cm^2 is caused by the localized accumulation of molecular damage over a threshold (~ 0.01 mm^2 in area around the crack tip), after which it gradually grows and leads to macroscopic fracture. Thus, the precursor we reported here takes place in an elastic and reversible form: if the load is released upon the detection of the precursor, the same region in the material will behave as there was never molecular damage.

The ability of MSDWS to detect and quantify displacements on short time scales and very small length scales –yet imaging a large field of view– is crucial for the early detection of the elastic response to localized damage. It distinguishes MSDWS from single scattering techniques and digital imaging correlation methods. These features make MSDWS a promising and convenient non-destructive tool for early-stage detection and prevention, especially for elastomers, where microscopic damage can be characterized by examining the elastic response in the *undamaged* region. Potentially, the performance of the detection of the localization by simple processing of ordinary low-resolution imaging could be largely enhanced with machine learning methods [55], and with a defined threshold for acceptable warning time, macroscopic fracture may be predictable even without knowing the details of the material.

Acknowledgments

This work was funded by the European Union's Horizon 2020 Programme for Research and Innovation under the Marie Skłodowska-Curie grant agreement no. 765811 (DoDyNet) and grant agreement AdG no. 695351 (CHEMECH). This work was partially supported by ANRT (grant no. 2014/0109) and ANR MultiNet (grant no. ANR-20-CE06-0028-01). LC gratefully acknowledges support from the Institut Universitaire de France. The authors thank Liangbin Li for kindly providing the natural rubber sample.

Data Availability

ASCII and tif. format images provided in all the figures in the main text and SI have been uploaded in Zenodo (DOI:10.5281/zenodo.6406808) [56].

APPENDIX A. Materials and methods

1. Material preparation

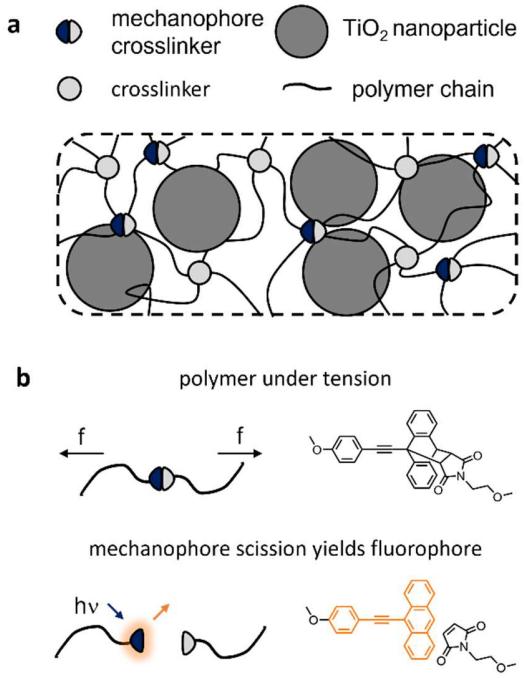

FIG. 10 (a) Material composition of PDMS with the addition of mechanophore crosslinker and nanoparticles. (The schematic is not to scale, since TiO_2 nanoparticle should be significantly larger than the mesh size) (b) Fluorescence mechanism of mechanophore crosslinker in polymer under tension.

PDMS elastomers were prepared from PDMS Sylgard 184 (Dow Corning) with a 10:1 ratio of PDMS base and curing agent. 4 g of PDMS base is first mixed with titanium dioxide (TiO_2) nanoparticles (diameter 250 nm, 10 mg) and sonicated for 10 minutes to avoid aggregation of the nanoparticles. Curing agent (0.4 g) and Diels-Alder adduct mechanophore (5 mg, dissolved in 1 g toluene) were then added and well mixed by vortexing for 10 minutes. The mixture is then poured in a mold to prepare a film and cured in vacuum at 90 °C for 8 hours, so that toluene can be evaporated during curing. The material composition is shown in FIG. 10(a). The synthesis of Diels-Alder adduct mechanophore (FIG. 10 (b)) was originally reported by Göstl et. al. [35] and described in detail in ref. [12]. As the mechanophore cross-linker is under tension and irreversibly broken, it becomes fluorescent under laser illumination with a wavelength of 405 nm, so that the accumulated bond scission can be quantified by measuring the fluorescence intensity [12,35].

2. Confocal microscopy

Confocal microscopy (Nikon AZ-100/C2+ confocal macroscope) is applied here to map 3D fluorescence intensity due to damage. We used an AZ Plan Fluor 5 × objective, with a focal length of 15 mm. The objective is zoomed by 3×, with a field of view 1.4 × 1.4 mm and image resolution of 0.68 μm/pixel (image size 2048 × 2048 pixel^2) in the plane. Excitation and emission collection wavelengths are 405 nm and 450 ~ 520 nm, respectively. In scanning confocal microscopy, a relatively long exposure time is required to acquire depth-resolved images with enough resolution and intensity, so that time resolution is poor. Furthermore, the fluorescence intensity of the activated mechanophore can be bleached after a long exposure under laser illumination. Considering the trade-off between image quality/time resolution and the need to avoid photobleaching, only four slices (thickness 150 μm with exposure time 8 s) are scanned for each 3D image, with a depth resolution of 200 μm and time resolution 2 min/scan, where images are collected at the beginning of each scan. The total scan thickness is 750 μm, situated around the midplane in the thickness direction of the sample. Quantification of the data is described in the **supplemental material**.

3. Multiple speckle diffusing wave spectroscopy

Time resolved imaging of the whole sample was simultaneously performed with MSDWS, with a better time resolution (100 ms) but a worse spatial resolution (size of the region of interest (ROI): 0.3 mm × 0.3 mm, magnification = 0.01 mm/pixel) compared to confocal microscopy. The technique detects motion in a sample slab of thickness several l^*, the photon transport mean free path [57]. In the present case, l^* is around 430 μm in the PDMS sample (20% of the sample thickness), measured in a suspension containing TiO_2 nanoparticles with the same volume concentration as in the elastomers [18]. For all MSDWS data except those of FIG. 7, the setup of FIG. 1(a) was used: the whole surface of the sample was illuminated homogeneously by an expanded green laser (wavelength 532 nm) and the speckle images were collected by a CMOS camera (BASLER acA2000-340km). The spatially resolved in-plane strain rate at the surface of the polymer network can be quantified from the autocorrelation function of the multiply scattered light intensity:

$$C_I(\vec{\boldsymbol{r}}, t, \tau) = \frac{\langle I_p(t) I_p(t+\tau)\rangle_{\vec{\boldsymbol{r}}}}{\langle I_p(t)\rangle_{\vec{\boldsymbol{r}}}\langle I_p(t+\tau)\rangle_{\vec{\boldsymbol{r}}}} - 1 \qquad (1)$$

t and τ are the experimental time and the time interval for correlation, respectively. $I_p(t)$ is the intensity at the p-th pixel and $\langle \dots \rangle_{\vec{\boldsymbol{r}}}$ provides the average over a ROI with a center position at $\vec{\boldsymbol{r}}$. The characteristic decorrelation time τ_0 of the autocorrelation function corresponds to the time over which the probe is displaced by $1/k$ (k is the wave vector), around 50 nm. At fixed t and $\vec{\boldsymbol{r}}$,τ_0 can be obtained by fitting C_I to [58]

$$C_I(\tau) = A exp\left(-2\gamma\sqrt{\left(\frac{\tau}{\tau_0}\right)^p + a}\right) + B \qquad (2)$$

and the characteristic decorrelation rate is defined as

$$\nu_0 = 1/\tau_0 \qquad (3)$$

This decorrelation rate can then be related to the deformation rate by

$$\nu_0 = \sqrt{3} k l^* \sqrt{f[\boldsymbol{D}]} \qquad (4)$$

, which is applied to visualize the two-dimensional (2D) strain rate distribution. $\boldsymbol{D}$ is the rate of deformation tensor [36] and $f[\boldsymbol{D}] = 2Tr(\boldsymbol{D}^2)/15$ [6,17]. Under uniform deformation in uniaxial tension, ν_0 can be directly related to true strain rate, as reported in ref. [18]. More details are shown in the **supplemental material**.

APPENDIX B. Simulated strain rate field close to the crack tip

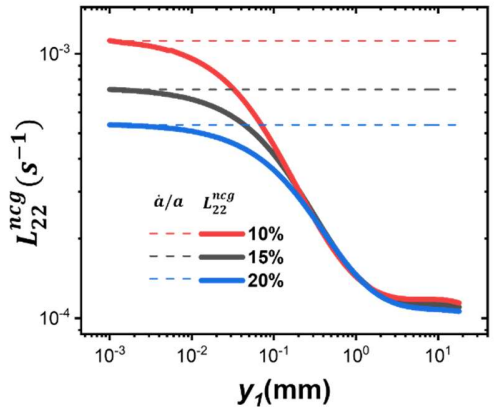

FIG. 11 $\boldsymbol{L}_{22}^{ncg}$ *(to be identified to* $D_{xx,FEM}$ *in the main text) and* $\dot{a}/a$ *at different* ε_N *plotted in a double logarithmic scale.*

$\boldsymbol{L}_{22}^{ncg}$ (ncg = no crack growth) at different ε_N are plotted in FIG. 11, corresponding to $D_{\mathrm{xx,FEM}}$ in the main text. The dash lines are the asymptotic result ($\dot{a}/a$ and $y_1 \to 0$) predicted by theory and determined numerically, as shown in Eq. 52 and FIG. S11(c), respectively in **supplemental material**. They are consistent with the FEM result obtained by computing the velocity gradient tensor directly. It is also discovered that: i) at far away from the tip ($y > 0.1$ mm), $\boldsymbol{L}_{22}^{ncg}$ is almost independent of ε_N; ii) at close to the tip ($y < 0.1$ mm), the slight decrease of $\boldsymbol{L}_{22}^{ncg}$ with increasing ε_N can be observed.

APPENDIX C. Dynamics analysis of delayed fracture under static condition

Under static condition, the bulk relaxation plays an important role in the dynamics measured by MSDWS, since the majority of the sample remains static during the measurement, free of the influence of the crack. The dynamics localized around the crack tip is influenced by both the bulk relaxation of the sample and the changes in elastic field due to the molecular damage. In this case, The DAM only provides a qualitative visualization of the degree of localization of the dynamics, rather than a quantitative mapping of the strain rate. To separate the effect of bulk relaxation and better visualize the damage/dynamics localization, we first fit the characteristic relaxation time τ_0 in Eq. 2 in regions far away from the crack tip and use τ_0 as a reference to choose τ_{MSDWS} . In this way, we estimate as precisely as possible the area having dynamics faster than in the bulk assuming that this faster activation is due to the presence of local damage.

1. The case of Poly (ethyl acrylate) elastomer

Poly (ethyl acrylate) (PEA) was synthesized through UV-initiated free radical polymerization following a previously reported procedure [27]. Ethyl acrylate monomer is mixed with TiO_2 nanoparticles (1 wt%), crosslinker 1,4-butanediol diacrylate (BDA, 0.5 mol%), UV initiator 2-Hydroxy-2-methylpropiophenone (1.16 mol%) and Diels-Alder adduct mechanophore diacrylate cross-linker (DACL) (0.02 mol%) [12]. The mixture is injected in a mold with thickness of 1 mm and polymerized under UV (10 $\mu W/cm^2$) for 2 hours. The Young's modulus is 0.47 MPa, measured by uniaxial extension (without notch). Due to the sedimentation of nanoparticles in the mixture with low viscosity, the final nanoparticle concentration in the bulk is less than 1 wt% and hard to quantify. The elastomer is then dried under vacuum overnight before usage, cut into rectangles and prenotched for single-edge notch fracture tests: length 10 mm between clamps, width of 6 mm and initial crack length of 1 mm. Frame rate is 5 s/scan.

We studied here only fracture behavior in static measurement since it provides an ideal condition for damage visualization in this soft material exhibiting little molecular damage in the bulk. The sample is loaded to ε_N = 15% and held for a long time for observation, with the set-up shown in FIG. 1(a). FIG. 12 (a) shows the activation intensity measured by confocal microscopy. A slight propagation is observed after 700 s, with an increasing fluorescence intensity around the crack tip.

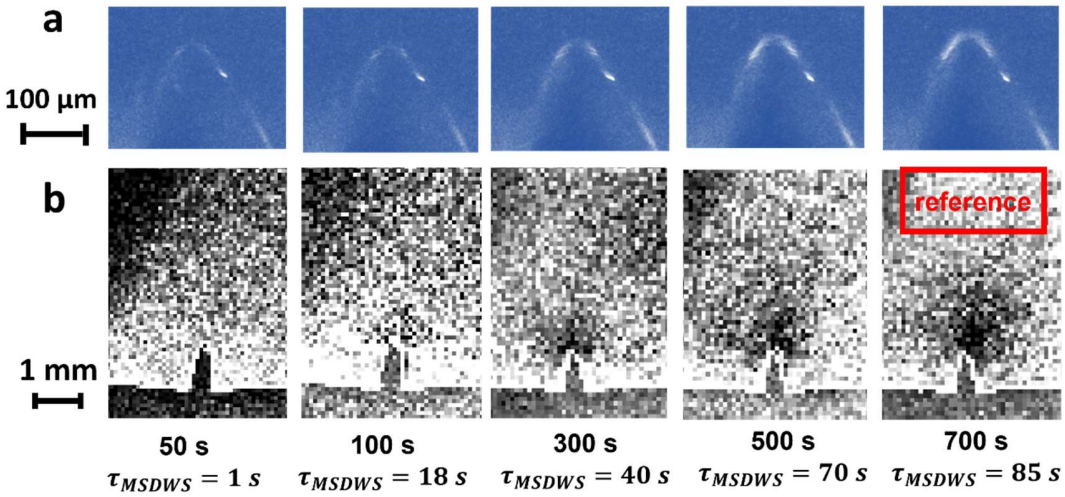

FIG. 12 Imaging of a poly (ethyl acrylate) sample after stretched to ε_N = 15%. (a) Mechanophore maps around the tip, measured by confocal microscopy and averaged over 50 s. (b) Dynamic activity maps (DAM) during the crack propagation, with τ_{MSDWS} fitted from the reference rectangular region. Each DAM is labelled by the corresponding t_w value.

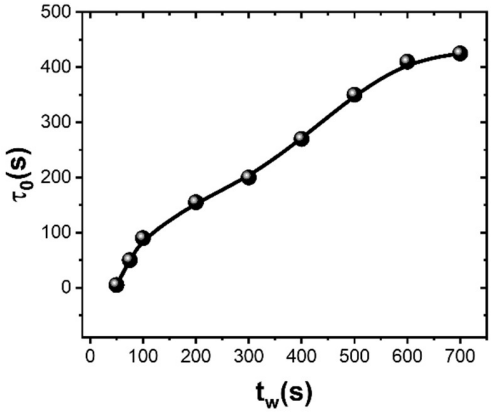

FIG. 13 Relaxation time τ_0 obtained by fitting Eq. 2 to the MSDWS data in the reference bulk region indicated in FIG. 12, as the function of t_w.

The relaxation time $\tau_0\,(t_w)$ obtained by fitting data from the reference region indicated in FIG. 12(b) is shown in FIG. 13. The relaxation time increases almost linearly with t_w, corresponding to the continuous slowing down of the bulk dynamics. DAMs with $\tau_{MSDWS} \approx 0.2\tau_0$ are converted into greyscale and shown in FIG. 12 (b), where the lower intensity in DAMs corresponds to faster dynamics. Fast dynamics (lower intensity) in DAMs can be detected over an initial surface around 1 mm^2 (t_w = 300 s) and grows to around 6 mm^2 at t_w = 700 s.

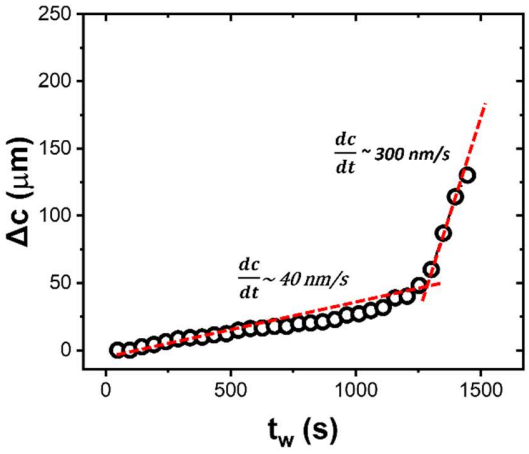

FIG. 14 Propagation length Δc as the function of t_w.

Even though the crack starts propagating right after the sample is deformed, the propagation is extremely slow, with less than 30 microns of increasing crack length over 1000 s. The increment of the crack length is calculated from mechanophore images and plotted in FIG. 14. An

acceleration of the rate of propagation of the crack can be observed after around t_w = 1200 s, where the propagation rate jumps from 40 nm/s to 300 nm/s. The sudden acceleration of crack propagation should be related to the accumulation of molecular damage from 0 to 1200 s, as seen in FIG. 12(a). The effect of a slight propagation during the first 1000 s can be decoupled from the accumulation of molecular damage, as pointed out in the FEM simulation.

2. The case of PDMS

The evolution of $\tau_0(t_w)$ in the bulk region of PDMS during the holding time at ε = 15% (FIG. 6) is shown in FIG. 15, which shows that in the bulk τ_0 exceeds several hundreds of s after t_w = 1000 s. Thus, the bulk dynamics are much slower to those related to a possible crack localization, and we can safely use τ_{MSDWS}= 40 s for all the DAM of FIG. 6(a). Although bulk dynamics is slowing with waiting time, the localized area around the crack with significantly faster dynamics than the bulk increases monotonically and the quantification in FIG. 6(b) is reliable.

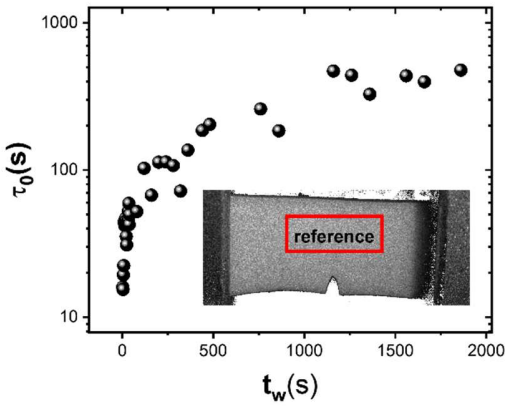

FIG. 15 Relaxation time τ_0 in the bulk region of PDMS in FIG. 6, as a function of t_w.

The change of crack length Δc is plotted in FIG. 16. The crack starts to slowly propagate (20 nm/s) at around 0.5 hour and slows down (to 3 nm/s) at around 1.5 h. In this example there is no macroscopic propagation leading to a macroscopic failure of the sample over the whole duration of the step (t_w = 5 h), although a longer observation time would have probably led to failure.

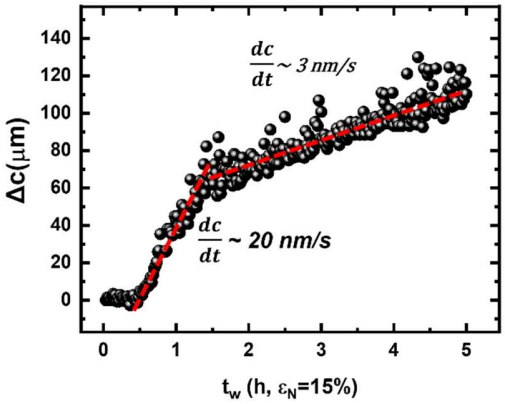

FIG. 16 Propagation length Δc as a function of t_w for the PDMS experiment of FIG. 6.

3. Sub-summary

Interestingly, when comparing the respective behaviors of PEA and PDMS, we find that a slower response in the fracture precursor of PDMS corresponds to a slowing down of the propagation (FIG. 16) at long time scales, while an earlier dynamics localization in PEA and its rapid growth correspond to an acceleration of the propagation (FIG. 14). Even though we are discussing here two totally different materials, this points out the possibility that the long-term behavior in delayed fracture can be predicted by the accumulation mode of the damage at a very early stage. A reliable model for this discussion needs more data and theoretical analysis, which is beyond the scope of this work.

APPENDIX D. Fracture precursor in PDMS with different modulus

Fracture precursors before crack propagation are measured in PDMS with different curing agent concentrations (Φ), varying from 0.0625 (15:1 of base/curing agent ratio) to 0.25 (3:1) (Φ is 0.091 (10:1) in the main text), using $\dot{\varepsilon}_N$ = 10^{-4} s^{-1}. All sample were cured at 90 °C for 8 hours. Critical strain for fracture ε_f and modulus at different Φ are plotted in Fig. 17. It can be found that modulus peaks at $\Phi \sim 0.12$, where ε_f is the lowest. The non-monotonic modulus as the function of Φ has been reported previously [59,60], and here by adjusting Φ, modulus can be tunable from around 0.6 MPa to 1.2 MPa.

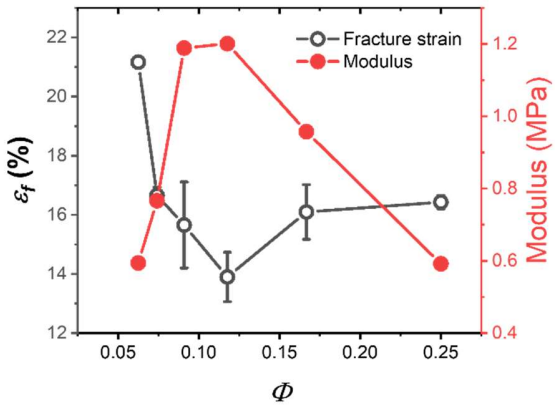

FIG. 17 Fracture strain ε_f and modulus as the function of curing agent concentrations Φ.

DAMs at 200 s before fracture can are shown in Fig. 18, with τ_{MSDWS} = 0.24 s. The sample size is 2 cm × 4 cm, with initial crack length of 2 mm. Fracture precursor with similar size and scale of the can be observed, with modulus and ε_f both change around twice.

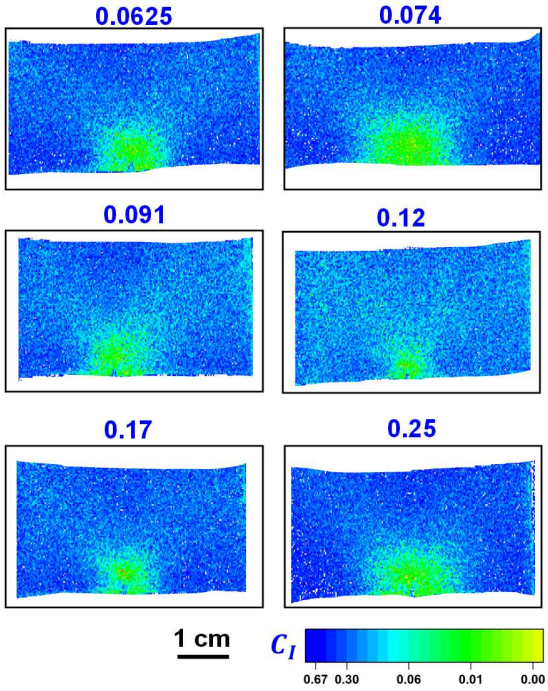

FIG. 18 DAM of single edge notched sample at 200 s before fractur, with τ_{MSDWS} = 0.24 s.

References

[1] C. Creton and M. Ciccotti, *Fracture and adhesion of soft materials: a review*, Rep. Prog. Phys. **79**, 046601 (2016).

[2] X. Wang and W. Hong, *Delayed fracture in gels*, Soft Matter **8** (2012).

[3] S. Mzabi, D. Berghezan, S. Roux, F. Hild, and C. Creton, *A critical local energy release rate criterion for fatigue fracture of elastomers*, J. Polym. Sci. B Polym. Phys. **49**, 1518 (2011).

[4] R. Bai, J. Yang, and Z. Suo, *Fatigue of hydrogels*, Eur. J. Mech. Solids **74**, 337 (2019).

[5] L. Vanel, S. Ciliberto, P.-P. Cortet, and S. Santucci, *Time-dependent rupture and slow crack growth: elastic and viscoplastic dynamics*, J. Phys. D **42** (2009).

[6] H. M. van der Kooij, S. Dussi, G. T. van de Kerkhof, R. A. Frijns, J. van der Gucht, and J. Sprakel, *Laser Speckle Strain Imaging reveals the origin of delayed fracture in a soft solid*, Sci. Adv. **4**, eaar1926 (2018).

[7] D. Bonn, H. Kellay, M. Prochnow, K. Ben-Djemiaa, and J. Meunier, *Delayed fracture of an inhomogeneous soft solid*, Science **280**, 265 (1998).

[8] X. Li, K. Cui, T. L. Sun, L. Meng, C. Yu, L. Li, C. Creton, T. Kurokawa, and J. P. Gong, *Mesoscale bicontinuous networks in self-healing hydrogels delay fatigue fracture*, Proc. Natl. Acad. Sci. **117**, 7606 (2020).

[9] I. Kolvin, J. M. Kolinski, J. P. Gong, and J. Fineberg, *How supertough gels break*, Phys. Rev. Lett. **121**, 135501 (2018).

[10] Y. Morishita, K. Tsunoda, and K. Urayama, *Velocity transition in the crack growth dynamics of filled elastomers: Contributions of nonlinear viscoelasticity*, Phys. Rev. E **93**, 043001 (2016).

[11] Y. Zhang, K. Fukao, T. Matsuda, T. Nakajima, K. Tsunoda, T. Kurokawa, and J. P. Gong, *Unique crack propagation of double network hydrogels under high stretch*, Extreme Mech. Lett. **51**, 101588 (2022).

[12] J. Slootman, V. Waltz, C. J. Yeh, C. Baumann, R. Göstl, J. Comtet, and C. Creton, *Quantifying rate-and temperature-dependent molecular damage in elastomer fracture*, Phys. Rev. X **10**, 041045 (2020).

[13] A. Duri, D. A. Sessoms, V. Trappe, and L. Cipelletti, *Resolving long-range spatial correlations in jammed colloidal systems using photon correlation imaging*, Phys. Rev. Lett. **102**, 085702 (2009).

[14] B. J. Berne and R. Pecora, *Dynamic light scattering: with applications to chemistry, biology, and physics* (Wiley, Hoboken, 1976).

[15] D. Weitz and D. Pine, in *Dynamic light scattering: The method and some applications* (Oxford University Press, Oxford, 1993), pp. 652.

[16] M. Erpelding, A. Amon, and J. Crassous, *Diffusive wave spectroscopy applied to the spatially resolved deformation of a solid*, Phys. Rev. E **78**, 046104 (2008).

[17] M.-Y. Nagazi, G. Brambilla, G. Meunier, P. Marguerès, J.-N. Périé, and L. Cipelletti, *Space-resolved diffusing wave spectroscopy measurements of the macroscopic deformation and the microscopic dynamics in tensile strain tests*, Opt. Lasers in Eng. **88**, 5 (2017).

[18] J. Ju, L. Cipelletti, S. Zoellner, T. Narita, and C. Creton, *Multispeckle diffusing wave spectroscopy as a tool to study heterogeneous mechanical behavior in soft solids*, J. Rheol. **66**, 1269 (2022).

[19] A. Duri, H. Bissig, V. Trappe, and L. Cipelletti, *Time-resolved-correlation measurements of temporally heterogeneous dynamics*, Phys. Rev. E **72**, 051401 (2005).

[20] S. Aime, L. Ramos, and L. Cipelletti, *Microscopic dynamics and failure precursors of a gel under mechanical load*, Proc. Natl. Acad. Sci. **115**, 3587 (2018).

[21] A. Pommella, L. Cipelletti, and L. Ramos, *Role of normal stress in the creep dynamics and failure of a biopolymer gel*, Phys. Rev. Lett. **125**, 268006 (2020).

[22] A. Le Bouil, A. Amon, S. McNamara, and J. Crassous, *Emergence of cooperativity in plasticity of soft glassy materials*, Phys. Rev. Lett. **112**, 246001 (2014).

[23] A. Furukawa and H. Tanaka, *Inhomogeneous flow and fracture of glassy materials*, Nat. Mater. **8**, 601 (2009).

[24] J. Diani, B. Fayolle, and P. Gilormini, *A review on the Mullins effect*, Eur. Polym. J. **45**, 601 (2009).

[25] Y. Merckel, J. Diani, M. Brieu, and D. Berghezan, *Experimental characterization and modelling of the cyclic softening of carbon-black filled rubbers*, Mater. Sci. Eng. A **528**, 8651 (2011).
[26] E. Ducrot, Y. Chen, M. Bulters, R. P. Sijbesma, and C. Creton, *Toughening elastomers with sacrificial bonds and watching them break*, Science **344**, 186 (2014).
[27] Y. Chen, C. J. Yeh, Y. Qi, R. Long, and C. Creton, *From force-responsive molecules to quantifying and mapping stresses in soft materials*, Sci. Adv. **6**, eaaz5093 (2020).
[28] Y. Chen, G. Mellot, D. van Luijk, C. Creton, and R. P. Sijbesma, *Mechanochemical tools for polymer materials*, Chem. Soc. Rev. **50**, 4100 (2021).
[29] X. P. Morelle, G. E. Sanoja, S. Castagnet, and C. Creton, *3D fluorescent mapping of invisible molecular damage after cavitation in hydrogen exposed elastomers*, Soft Matter **17**, 4266 (2021).
[30] G. E. Sanoja, X. P. Morelle, J. Comtet, C. J. Yeh, M. Ciccotti, and C. Creton, *Why is mechanical fatigue different from toughness in elastomers? The role of damage by polymer chain scission*, Sci. Adv. **7**, eabg9410 (2021).
[31] J. Slootman, C. J. Yeh, P. Millereau, J. Comtet, and C. Creton, *A molecular interpretation of the toughness of multiple network elastomers at high temperature*, Proc. Natl. Acad. Sci. **119**, e2116127119 (2022).
[32] H. Liebowitz and E. Moyer Jr, *Finite element methods in fracture mechanics*, Comput. Struct. **31**, 1 (1989).
[33] V. R. Krishnan, C. Y. Hui, and R. Long, *Finite strain crack tip fields in soft incompressible elastic solids*, Langmuir **24**, 14245 (2008).
[34] J. M. Clough, C. Creton, S. L. Craig, and R. P. Sijbesma, *Covalent bond scission in the Mullins effect of a filled elastomer: real - time visualization with mechanoluminescence*, Adv. Funct. Mater. **26**, 9063 (2016).
[35] R. Göstl and R. Sijbesma, *π-extended anthracenes as sensitive probes for mechanical stress*, Chem. Sci. **7**, 370 (2016).
[36] G. T. Mase, R. E. Smelser, and G. E. Mase, *Continuum mechanics for engineers* (CRC press, Boca Raton, 2009).
[37] G. C. Johnson and D. J. Bammann, *A discussion of stress rates in finite deformation problems*, Int. J. Solids Struct. **20**, 725 (1984).
[38] T. J. Hughes and J. Marsden, *Mathematical foundations of elasticity* (Courier Corporation, North Chelmsford, 1994).
[39] D. André, *pydic*, https://gitlab.com/damien.andre/pydic (2018).
[40] S. R. Lavoie, R. Long, and T. Tang, *A rate-dependent damage model for elastomers at large strain*, Extreme Mech. Lett. **8**, 114 (2016).
[41] R. Long, V. R. Krishnan, and C.-Y. Hui, *Finite strain analysis of crack tip fields in incompressible hyperelastic solids loaded in plane stress*, J. Mech. Phys. Solids **59**, 672 (2011).
[42] G. Lake and A. Thomas, *The strength of highly elastic materials*, Proc. Math. Phys. Eng. Sci. **300**, 108 (1967).
[43] J. D. Valentin, X.-H. Qin, C. Fessele, H. Straub, H. C. van der Mei, M. T. Buhmann, K. Maniura-Weber, and Q. Ren, *Substrate viscosity plays an important role in bacterial adhesion under fluid flow*, J. Colloid Interface Sci. **552**, 247 (2019).
[44] J. M. Clough, C. Creton, S. L. Craig, and R. P. Sijbesma, *Covalent Bond Scission in the Mullins Effect of a Filled Elastomer: Real-Time Visualization with Mechanoluminescence*, Adv. Funct. Mater. **26**, 9063 (2016).
[45] C. Lee, W. A. Take, and N. A. Hoult, *Optimum accuracy of two-dimensional strain measurements using digital image correlation*, J. Comput. Civ. Eng. **26**, 795 (2012).
[46] A. Acciaioli, G. Lionello, and M. Baleani, *Experimentally achievable accuracy using a digital image correlation technique in measuring small-magnitude (< 0.1%) homogeneous strain fields*, Materials **11**, 751 (2018).
[47] M. Sutton, J. Turner, H. Bruck, and T. Chae, *Full-field representation of discretely sampled surface deformation for displacement and strain analysis*, Exp. Mech. **31**, 168 (1991).
[48] B. Winiarski, G. Schajer, and P. Withers, *Surface decoration for improving the accuracy of displacement measurements by digital image correlation in SEM*, Exp. Mech. **52**, 793 (2012).
[49] M. Liu, J. Guo, C. Y. Hui, and A. T. Zehnder, *Application of Digital Image Correlation (DIC) to the Measurement of Strain Concentration of a*

PVA Dual-Crosslink Hydrogel Under Large Deformation, Exp. Mech. (2019).
[50] R. Sedlacek and F. A. Halden, *Method for tensile testing of brittle materials*, Rev. Sci. Instrum. **33**, 298 (1962).
[51] S. L. Phoenix and R. G. Sexsmith, *Clamp effects in fiber testing*, J. Compos. Mater. **6**, 322 (1972).
[52] M. Y. Nagazi, P. Dieudonné-George, G. Brambilla, G. Meunier, and L. Cipelletti, *Phase transitions in polymorphic materials probed using space-resolved diffusing wave spectroscopy*, Soft matter **14**, 6439 (2018).
[53] S. Lee and M. Pharr, *Sideways and stable crack propagation in a silicone elastomer*, Proc. Natl. Acad. Sci. **116**, 9251 (2019).
[54] C. Marano, M. Boggio, E. Cazzoni, and M. Rink, *Fracture phenomenology and toughness of filled natural rubber compounds via the pure shear test specimen*, Rubber Chem. Technol. **87**, 501 (2014).
[55] V. Bapst *et al.*, *Unveiling the predictive power of static structure in glassy systems*, Nat. Phys. **16**, 448 (2020).
[56] *ASCII and images of all the datasets shown in the figures in the main text and Supplemental Material have been deposited in Zenodo, doi: 10.5281/zenodo.6406808*
[57] D. J. Pine, D. A. Weitz, P. M. Chaikin, and E. Herbolzheimer, *Diffusing wave spectroscopy*, Phys. Rev. Lett. **60**, 1134 (1988).
[58] F. Cardinaux, L. Cipelletti, F. Scheffold, and P. Schurtenberger, Microrheology of giant-micelle solutions, EPL 57, 738 (2002).
[59] H. Hocheng, C.-M. Chen, Y.-C. Chou, and C.-H. Lin, Study of novel electrical routing and integrated packaging on bio-compatible flexible substrates, Microsyst. Technol. 16, 423 (2010).
[60] M. L. Fitzgerald, S. Tsai, L. M. Bellan, R. Sappington, Y. Xu, and D. Li, The relationship between the Young's modulus and dry etching rate of polydimethylsiloxane (PDMS), Biomed. Microdevices 21, 1 (2019).